



# Tool wear monitoring based on the combination of machine vision and acoustic emission

Meiliang Chen<sup>1</sup> · Mengdan Li<sup>1</sup> · Linfeng Zhao<sup>1</sup> · Jiachen Liu<sup>1</sup>

Received: 15 August 2022 / Accepted: 28 January 2023 / Published online: 3 February 2023  
© The Author(s), under exclusive licence to Springer-Verlag London Ltd., part of Springer Nature 2023

## Abstract

Tool condition monitoring (TCM) has developed several mature methods to improve processing efficiency. However, existing methods either require the removal of the tool from the machining system for individual monitoring or extensive data processing, manual labeling, and empirical judgment on whether to replace the tool. A TCM method combining machine vision and acoustic emission (AE) is proposed in this paper. Based on the structural similarity index (SSIM) algorithm, the relationship between tool speed and camera frame number is established. Through machine learning (ML) and neural network (NN) methods, the mapping between the wear mount extracted by the machine vision method and the AE feature vector is constructed, and the tool monitoring model is established. Verified by the data set obtained by the milling test, the TCM model established by the proposed can achieve a recognition accuracy of 96.11%, and the root mean square error (RMSE) predicted by the model is 0.0106. This method has proved to be practical and versatile in TCM.

**Keywords** Tool condition monitoring · Machine vision · Acoustic emission · Machine learning · Neural network

## 1 Introduction

With the introduction of Industry 4.0, intelligent manufacturing has become the dominant direction of modern manufacturing transformation [1]. In the intelligent machining of CNC machine tools, TCM plays an essential role in the quality and efficiency of precision cutting machining of parts [2]. During the cutting process, the tool is constantly in contact with the workpiece, which inevitably causes wear, especially for various difficult-to-machine materials in the aerospace field often have high cutting resistance and low thermal conductivity, which are more likely to cause tool wear than other materials [3]. It is estimated that 20% of machine downtime is caused by tool breakage, while the cost of the tool itself

and the cost of replacing it account for 3–12% of the total cost [4, 5]. CNC machines equipped with accurate and reliable TCM systems can increase total production by 10 to 50% and reduce total processing costs by 10–40% [6]. TCM system has been paid much attention to and studied by people because it not only improves the utilization of tools but also reduces problems of machine failure and obsolescence caused by tool failure [7].

Generally, TCM technology has two methods: direct and indirect monitoring [8]. The direct monitoring method requires the tool to be removed separately from the machine system. Then, the tool flank wear width, crater depth, and crater area are obtained using optical instruments or machine vision methods [9]. Fernández-Robles et al. [10] processed and analyzed the micro milling tool images based on various image processing algorithms to predict the tool wear status, solving the challenge of the difficulty of directly measuring worn tools. Zhang et al. [11] proposed a visual fusion method combining machine learning and image processing to detect minor defects in helical cutting edges. Fong et al. [12] proposed a tool wear detection system based on correlation analysis and quantitative images. You et al. [13] proposed a tool state image sequence (TCIS) based on continuous images, based on which adaptive online monitoring of milling cutters was achieved by using prior knowledge

✉ Mengdan Li  
l875661574@163.com

Meiliang Chen  
mlchen18@163.com

Linfeng Zhao  
linfengzhao96@163.com

Jiachen Liu  
liujiachen7@163.com

<sup>1</sup> School of Mechanical Engineering, Xiangtan University, Xiangtan 411105, China

and neighborhood search to locate and track tool wear region locations. Miao et al. [14] constructed a U-Net-based tool wear region monitoring network and introduced depth supervision to solve the problem's few shots and data imbalance. More and more research is beginning to combine machine vision and machine learning to solve the problem of insufficient sample size and low accuracy of direct monitoring methods. However, while direct monitoring methods can monitor tool wear and tear through direct measurements, they can also be interfered with by field conditions, cutting fluid, and cutting chips. Most direct monitoring methods require machine halt measurement. This issue directly impacts the accuracy and efficiency of direct monitoring methods online. Therefore, direct monitoring methods are not widely used in manufacturing.

In recent years, many researchers have devoted themselves to the indirect monitoring of tool conditions with the development of computer information technology and sensor-related technology. Dou et al. [15] proposed a method of establishing a TCM model based on cutting force and vibration signals using a sparse self-encoder model. The results show that this method can effectively monitor the wear state of the tool online under different cutting conditions. Móricz et al. [16] used neural networks to monitor tool wear online and offline during ceramic processing through spindle power signal and vibration analysis. Kong et al. [17] used the correlation coefficient method and kernel principal component analysis (KPCA) method to analyze the cutting force signal and a tool wear prediction model based on support vector regression. The model has good prediction accuracy and generalization ability under minor sample conditions. Laddada et al. [18] developed a tool life prediction model using complex continuous wavelet transform (CCWT) and an improved extreme learning machine (IELM). Gao et al. [19] proposed a multi-sensor mixed domain information fusion method for tool wear prediction by performing wavelet packet decomposition and feature fusion on the collected multi-sensor signals and building a model using gated recurrent unit (GRU) for dynamic prediction of tool wear. Huang et al. [20] proposed a tool wear prediction method based on deep convolutional neural network (DCNN) multi-domain feature fusion. This method extracts time, frequency, and time–frequency domain characteristics from the collected multi-sensory signals and uses DCNN to build a tool wear prediction model. As the above research shows, combining multi-sensor fusion and machine learning has become a hot trend in TCM. Although the multi-sensor fusion method makes the existing TCM system more stable and accurate, it inevitably produces problems such as a large amount of data, complex information, and manual labeling.

To solve the problems of a single monitoring method, the efficiency of TCM is further improved. This paper proposes a TCM method based on machine vision and the AE method.

The method is executed in the following steps. Firstly, the image collected by machine vision is processed to obtain the wear amount of the milling cutter. Then, the collected AE signals are extracted, filtered, and fused to construct the AE feature vector. Secondly, the wear amount obtained by the machine vision method is used as the label of the AE feature vector, and the mapping between them is established by the machine learning method. Finally, BP neural network, Elman neural network, and support vector machine (SVM) model are optimized by the ABC algorithm to establish a combined tool wear monitoring model. The data samples are obtained by milling experiments. The established combined model is compared with a single neural network and machine learning model, which proves that the established combined model has the best overall performance. In addition, this paper also proposes an automatic online tool image acquisition method. The automated online acquisition of the tool image is realized by establishing the relationship between the number of frames collected by the camera and the tool speed, and the SSIM algorithm is used to select the best image.

## 2 Tool wear monitoring system

### 2.1 Tool wear monitoring platform

The tool wear monitoring platform is shown in Fig. 1, divided into hardware and software. The hardware part includes visual acquisition and acoustic emission signal acquisition. Among them, the visual acquisition includes a focusing lens, ring LED light source, CCD camera, camera bracket, and computer; and the AE signal acquisition part includes an AE sensor, amplifier, and instrument. The software consists of image processing, AE signal processing, and a tool wear monitoring model. The tool wear monitoring system obtains the tool wear value through the vision processing module. The eigenvectors representing tool wear extracted from the acoustic emission signals are then marked with wear values. Then, a sample set with wear value labels is established, which provides a guarantee for the accuracy and applicability of the tool wear monitoring model.

### 2.2 Tool monitoring system process

The system's workflows are shown in Fig. 2. As shown in Fig. 1, the camera of the optical module is fixed to the machine tool's work platform and moves with the work platform. Before the start of the processing, it is necessary to debug the best image acquisition conditions and set the acquisition points and acquisition intervals that the tool needs to return through the CNC programming of the machine tool. After processing begins, the AE instrument

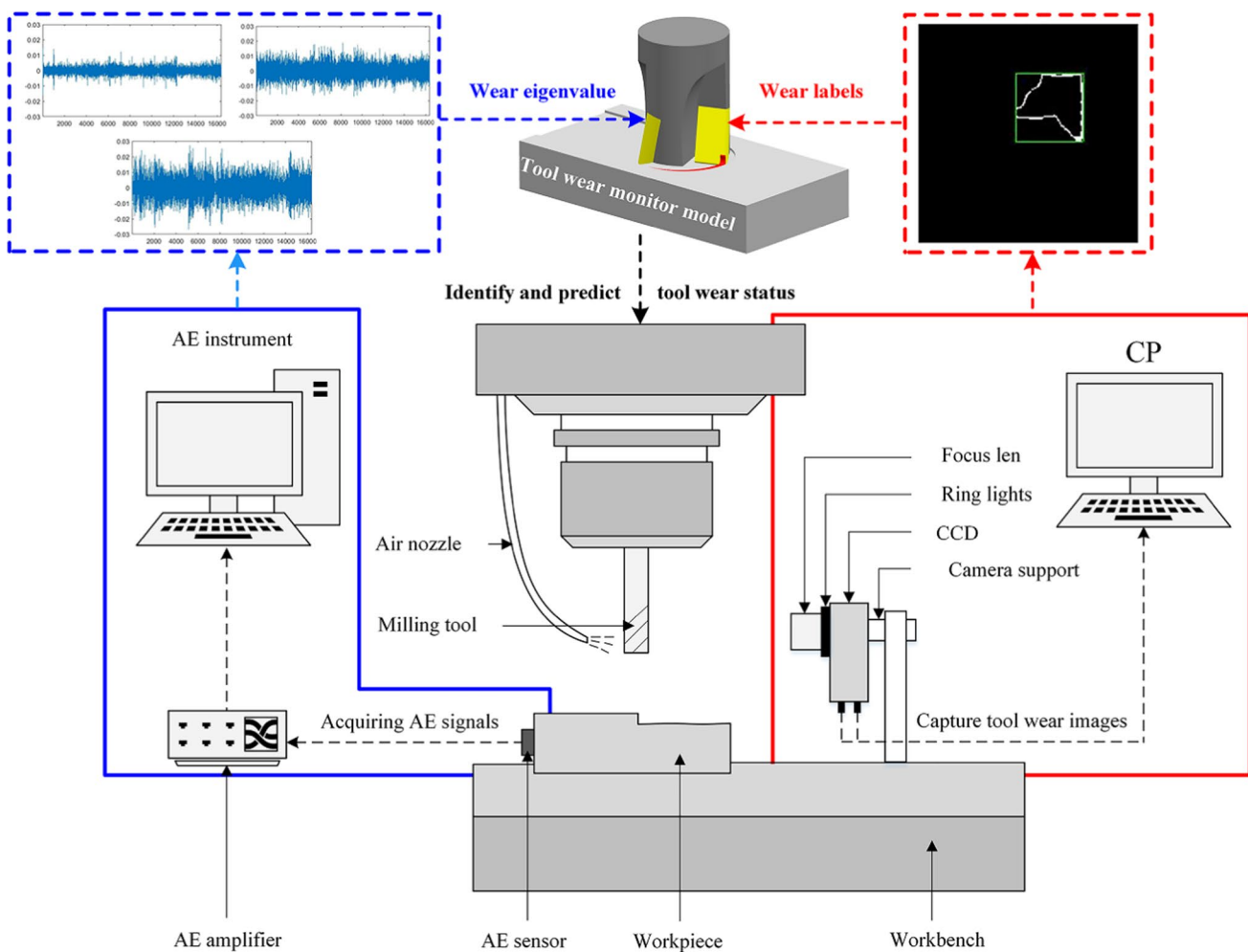


**Fig. 1** Schematic diagram of tool wear monitoring platform

continuously collects the emission signal through a sensor attached to the side of the workpiece. When the program reaches the set interval time, the tool returns to the acquisition point and rotates at a specific, smaller speed to facilitate image acquisition. After the acquisition, the image is processed, the tool wear value is extracted, and the wear value is used as a marker for the acoustic emission signal corresponding to the time interval of the image acquisition. The acoustic emission signal is processed, and the tool wear characteristic value is obtained. Finally, the tool wear monitoring model is established to identify and predict tool wear status and life. Stop and replace the tool when the model confirms that the tool has met the blunt standard.

### 2.3 Experimental platform building

According to the tool wear monitoring platform, the image and signal acquisition device shown in Fig. 3 is set up in MVC 650 NC milling machine. The workpiece is GH4169

nickel-based alloy, 120 mm × 60 mm × 35 mm. R390-11T3 04E-PL S30T CoroMill R390 020A20-11Mde Sandvik 3-tooth handle and TiAlN-coated carbide inserts were used for milling experiments. A CCD camera model Cognex In-Sight 5403 with Fujinon CF25HA-1 focus lens and Cognex P/N 119-2043R LED ring light source was used for image acquisition. In addition, to verify the accuracy of the wear extracted by the image processing module, it is necessary to measure the wear using the handheld microscope model Dino-light AM4113T. The AE signals are collected and processed using PCI-2 and AE-win software and are equipped with sensors and amplifiers.

### 2.4 Test scheme

In this paper, milling tests are conducted using milling parameters, as shown in Table 1. Two groups of different cutting parameters were set for the milling test, and the milling method was down milling. Since the number

**Fig. 2** Tool wear monitoring process

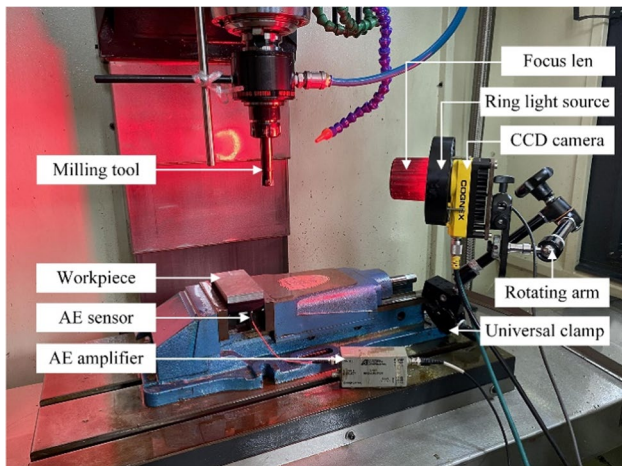
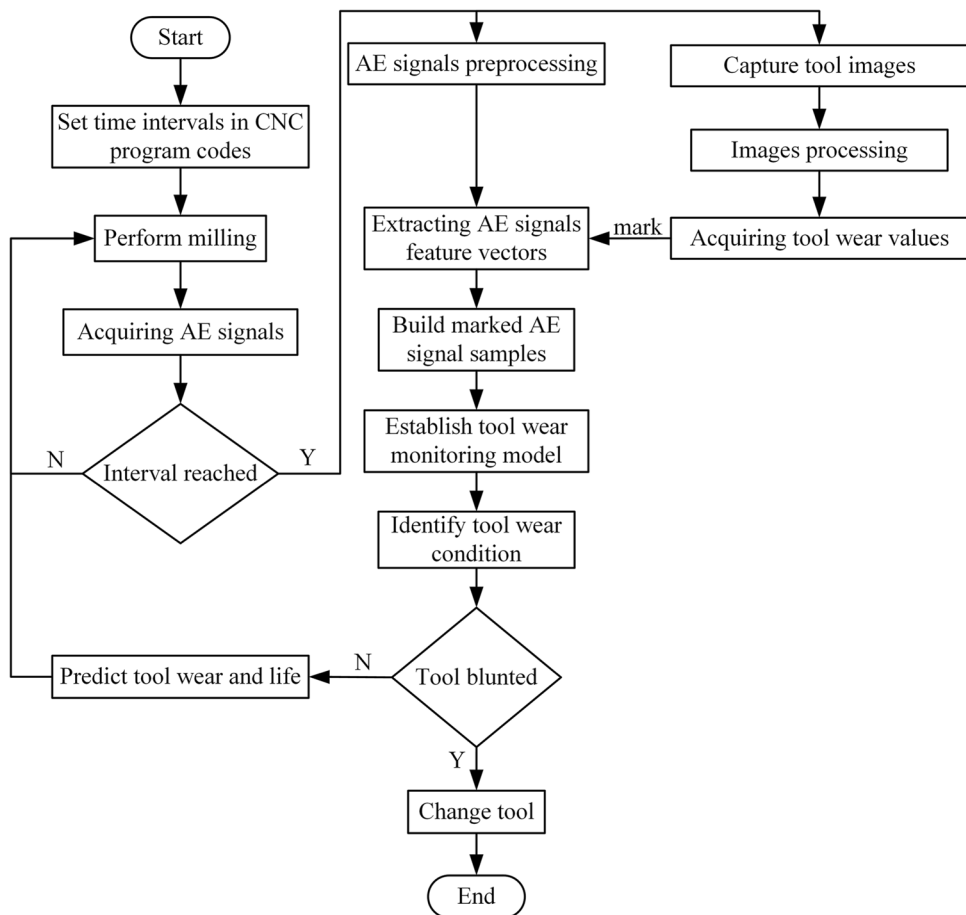


**Fig. 3** Test device

of tool walk  $T$  has the greatest impact on tool wear, multiple levels are set for this factor. To detect the calculation accuracy of the visual module under different wear conditions, the test used 16 groups of the same carbide inserts. The inserts were divided into two groups for eight

**Table 1** Milling test parameters

Name of test parameters	Test parameter values
Milling speed $v$ (m/min)	40, 60
Feed per tooth $f_z$ (mm/z)	0.15, 0.2
Axial cutting depth $a_p$ (mm)	0.3
Number of tool walk $T$	20, 40, 60, 80, 100, 120, 140, 160

milling experiments with different cutting times after the completion of milling by handheld microscope detection. To collect enough samples for the model establishment, ten groups of milling tests with cutting times  $T = 160$  were carried out in two groups of cutting parameters, and images and AE signals were collected. During the machining process, the AE signals were collected without interruption, and the tool was returned to the image acquisition point for image acquisition every 20 tool passes.

## 2.5 Automatic online image acquisition method

In the actual image acquisition, due to the tool's speed, the insert's flank face cannot be directly in front of the CCD camera, so it is not easy to obtain a qualified image of the flank face of the tool. Therefore, this paper proposes an automatic image acquisition and screening method based on the SSIM algorithm [21], which automatically collects images of all inserts of milling cutters online and controls the image quality to an acceptable range.

The image obtained when the camera faces the tool flank face is standard. The SSIM is used as the quality evaluation index for the acquired image. The similarity between the acquired image and the standard image is calculated, and then, the quality of the acquired image is evaluated. The formula for calculating the structural similarity is as follows.

$$SSIM(x, y) = \frac{(2u_x u_y + C_1)(2\sigma_{xy} + C_2)}{(u_x^2 + u_y^2 + C_1)(\sigma_x^2 + \sigma_y^2 + C_2)} \quad (1)$$

where  $x$  is the acquired image, and  $y$  is the standard image;  $u_x$ ,  $u_y$ ,  $\sigma_x$ ,  $\sigma_y$ , and  $\sigma_{xy}$  are the mean, standard deviation, and covariance between  $x$  and  $y$  images; and  $C_1$ ,  $C_2$ , and  $C_3$  are constants with small values to avoid the tendency of the denominator to 0 when describing low brightness and contrast, which results in inconsistent measurement results. The SSIM's value domain is  $[-1, 1]$ . The higher the image quality obtained, the closer the value is to 1. Otherwise, the closer the value is to -1. The similarity  $r$  calculation formula is as follows.

$$r = \frac{SSIM(x, y) + 1}{2} \times 100\% \quad (2)$$

The tool rotates at a certain speed during image acquisition. To determine the initial threshold values  $[\gamma_{\min}, \gamma_{\max}]$  of the rotation angle of the tool between the two collected images, the tool image collected with the tool flank face facing the camera is used as the standard image. Set the tool rotation angle  $r$  range to  $-10^\circ$  to  $10^\circ$  with an increment of  $2^\circ$ , gradually rotate the tool, and capture the image. The tool rotation angle's initial threshold  $[\gamma_{\min}, \gamma_{\max}]$  is then determined by calculating the  $r$  value of the resulting image.

To reduce contingency, six sets of blades are used for image acquisition, and the results are shown in Fig. 4. As can be seen from the figure, when  $-8^\circ \leq \gamma \leq 8^\circ$ , the  $r$  value of all six groups of leaves was greater than 95%. Therefore, the tool rotation angle threshold is determined to be  $[-8^\circ, 8^\circ]$ .

Then, the minimum interval angle  $\varphi$  of image acquisition is determined, that is, the minimum interval angle of two adjacent images. To obtain a high-quality image, the  $\varphi$  should satisfy the following equations.

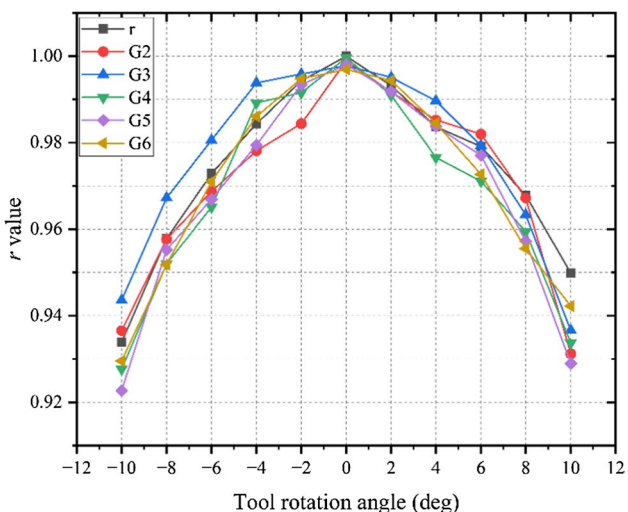


**Fig. 4** Tool rotation angle and  $r$  value relationship

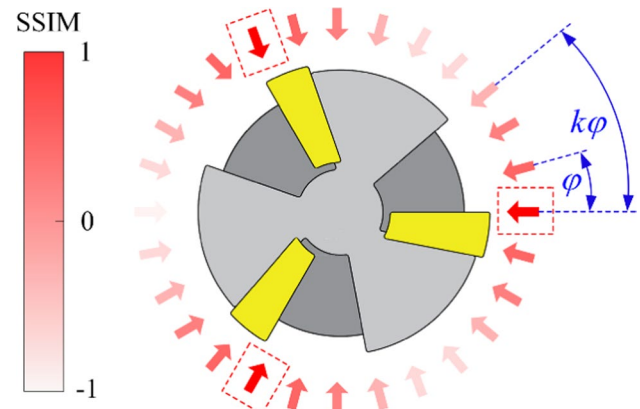


**Fig. 5** Image acquisition angle and image similarity at each angle

$$\varphi = \frac{360^\circ}{tF} \quad (3)$$

$$\varphi \leq \gamma_{\max} - \gamma_{\min} \quad (4)$$

where  $t$  is the time required to perform image acquisition, and  $F$  is the number of camera frames, i.e., the number of images collected in 1 s. The CCD camera used in this paper can acquire 14 images in 1 s. Considering the excessive transmission of images on the computer load and the effect of the timeliness, set  $F = 7$ . Get  $t \geq 3.214\text{s}$  and take  $t = 4\text{s}$  for 28 images with a minimum image acquisition interval angle  $\varphi = 12.857^\circ$ .

For ease of expression, the following assumptions are made. It is assumed that the tool is fixed during image acquisition, and the camera rotates around it. The angles of image acquisition and the similarity of each angle are shown in Fig. 5. The arrow indicates the image acquired from each angle, and the

darker the arrow's color, the higher the SSIM value of the image acquired from that angle to the standard image. It can be seen from the image that the similarity of each blade image of the milling cutter is greater than 95% of the standard image when the image is obtained from  $\varphi$  angle or a certain multiple of  $k\varphi$  as an interval angle. Thus, the relationship between spindle speed  $n$  and minimum interval angle  $\varphi$  in the image acquisition process is given.

$$n = \frac{60(Ft - 1)k\varphi}{360t} \quad (5)$$

where  $k$  is a specific integer between 0 and 28; it is subject to the following constraints.

- (1)  $k$  belongs to the set of numbers  $K = \{k|0 < k < 28, k \in Z\}$ .
- (2) If the current image acquisition angle is the same as the acquired angle, discard the  $k$  value.
- (3) After the first image is collected from its original position, the basic angle unit is the angle of  $\varphi$ . After the angle of  $k\varphi$  is increased 27 times, the image acquisition angle should include all the angles shown in the arrow in Fig. 5.

To solve Eq. (5), the possible values of the interval angle factor  $k$  and the spindle speed  $n$  can be obtained, as shown in Table 2.

The speed values in the table are ideal because the CCD camera can still acquire a clear picture of an object when shooting at 450 km/h. In this paper, we used spindle speed  $n = 130.18$  rpm to image acquisition at  $k = 9$ , then sequenced the 28 images collected with SSIM values, and selected the three images with the highest SSIM value as the best images for each cutting blade. High-quality images of all milling cutter blades can be obtained automatically.

### 3 Extraction of tool wear

#### 3.1 Blunt standard of tools

In ISO 8668–2, flank wear width  $VB$  is recommended as the standard for tool life. In different stages of tool wear,  $VB$  has its characteristics and different development trends. Therefore, the average value of  $VB$ ,  $VBave$ , is used as a quantitative indicator of tool wear. For different workpiece materials, the wear standard is usually different. In practice, the degree of wear can be determined according to the working conditions. Since the

nickel-based alloy GH4169 was used as the test's workpiece, a blunt standard of tools, as shown in Table 3, is used in this paper [21].

#### 3.2 Image acquisition

##### 3.2.1 Image cropping

The tool image obtained contains a large amount of data information, of which only the tool noise belongs to the region of interest (ROI). In order to reduce the increase in computing overhead caused by unrelated areas, tool images must be cropped. In this paper, ROI identified by feature from accelerated segment test (FAST) feature point detection and the coordinate mean of the ten feature points with the highest vertical orientation is used as the selected feature points [22]. The ROI is obtained by cropping the 161 × 161 pixel neighborhood of the selected feature point, as shown in Fig. 6.

##### 3.2.2 Image denoising and enhancement

Because the unprocessed cropped tool image is disturbed by the ambient noise, the image quality is poor, and the boundary of the worn area is blurred. As shown in Fig. 7a, the presence of a large number of noise points in the original image interferes with the subsequent extraction of the tool's wear contour and affects the accuracy of wear calculation. The denoising and enhancement methods in Reference [21] are used to process the image. The results are shown in Fig. 7b and c.

#### 3.3 Wear edge extraction

##### 3.3.1 Threshold segmentation

We choose the Otsu method, widely used in research, to divide tool images by threshold [23]. The result is shown in Fig. 8.

**Table 3** Blunt standard of tools

Tool wear condition	Wear amount of rear blade surface
Initial wear	$VBave \leq 0.1\text{mm}$
Normal wear	$0.1\text{mm} \leq VBave \leq 0.25\text{mm}$
Severe wear	$VBave \geq 0.25\text{mm}$

**Table 2** Spacing angle coefficient  $k$  and spindle speed  $n$

$k$	1	3	5	9	11	13	15	17	19	23	25	27
$n/\text{rpm}$	14.46	43.39	72.32	130.18	159.11	188.03	216.96	245.89	274.82	332.67	361.6	390.53

**Fig. 6** Image cropping based on FAST feature points

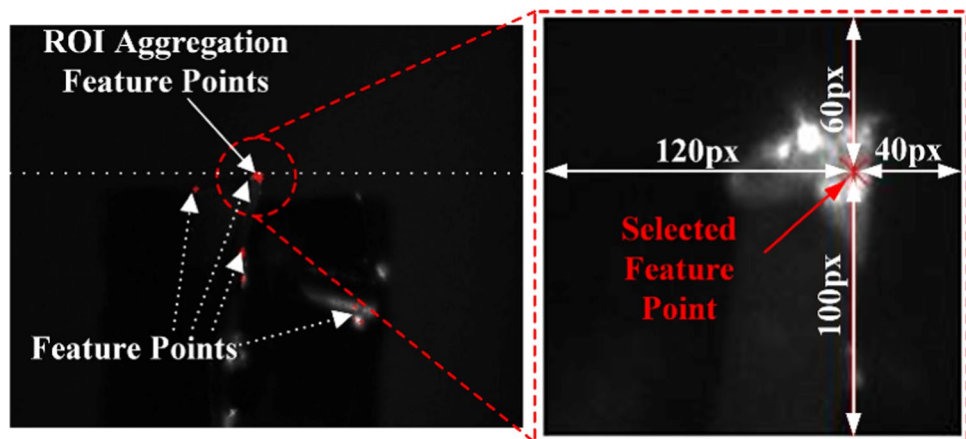


**Fig. 7** Image of tool wear area.  
a Original image, b denoising image, c enhance image

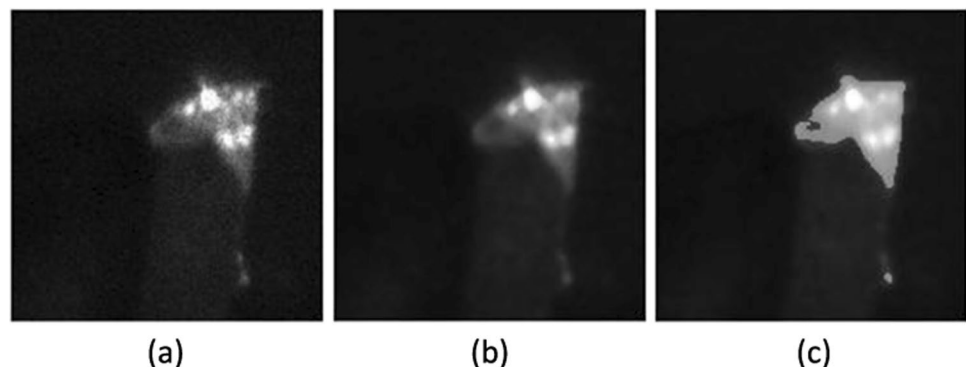


**Fig. 8** Threshold segmentation result

### 3.3.2 Wear area optimization and edge detection

The image after threshold segmentation has external and irregular wear problems. The wear area was optimized by the binary morphological method [21]. The result is shown in Fig. 9a. Finally, edge detection is performed using the Canny operator [24]. The edge detection result is shown in Fig. 9b. The wear edges detected using the Canny operator can be seen to be clear and complete.

## 3.4 Extraction of wear amount

### 3.4.1 Image correction

As shown in Fig. 10, since the main cutting edge of the tool is not vertical, there is some error in comparing the measurement of wear width to the actual wear width when conducting a line scan. Therefore, the image must be calibrated to obtain more accurate calculation results.

In this paper, the tool's main cutting-edge straight line is obtained using the Hough transform linear detection method

**Fig. 9** Image edge extraction.  
**a** Morphologically processed image. **b** Edge detection image

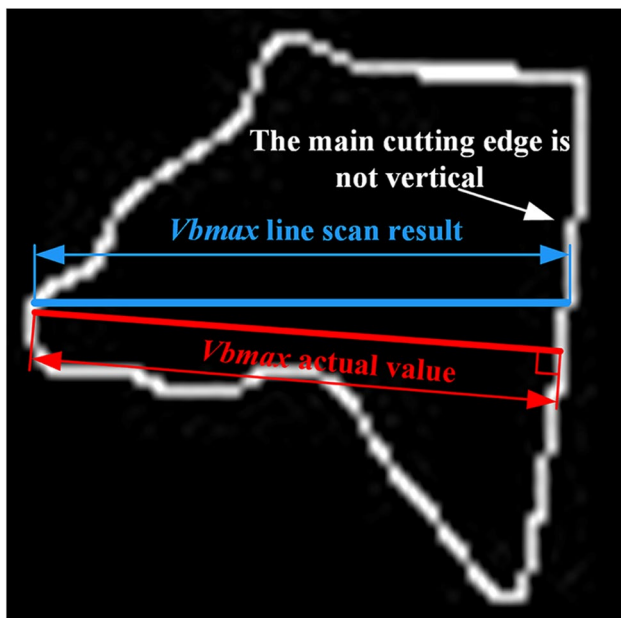
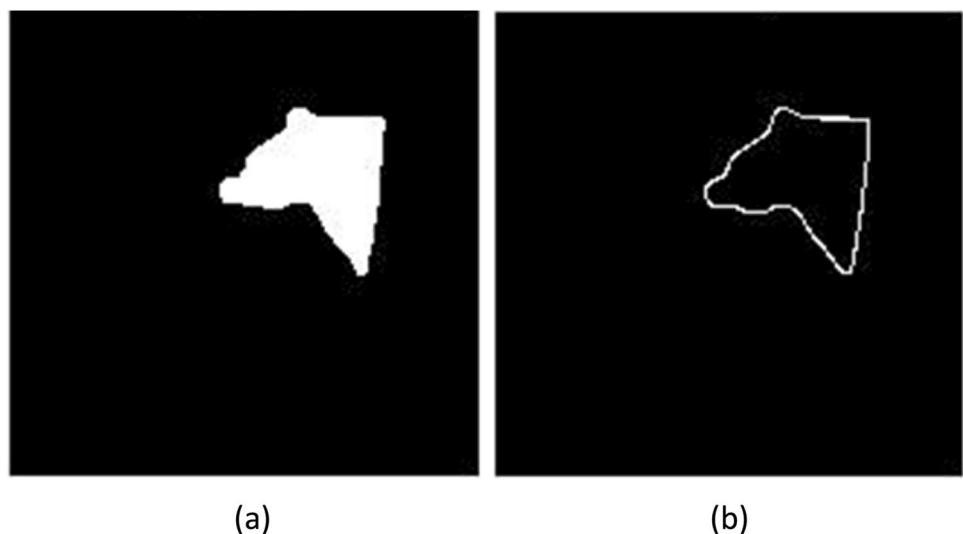


**Fig. 10** Error source of wear volume extraction

[25]. The angle  $\theta$  between the main cutting edge and the vertical line is obtained through Hough transform, and then, the image is rotated by an angle of  $\theta$ . That is, the vertical image of the main cutting edge is obtained.

Hough transform mainly uses polar coordinates to represent straight lines. By transforming the pixel points  $(i, j)$  in the pixel rectangular coordinate space of the image to the parameters  $(\rho, \varphi)$  in the polar coordinate space, the line detection in the image is converted into finding a point in polar coordinates that passes through the most sine curve.

The specific form of space conversion is shown in formula (6).

$$\rho = i \cos \varphi + j \sin \varphi \quad (6)$$

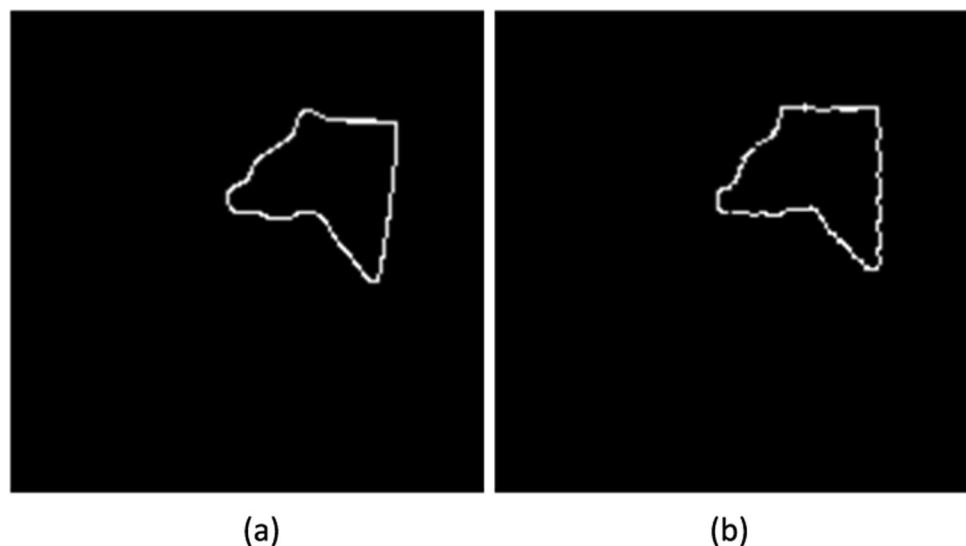
The entire image correction process is as follows:

- 1) Use Hough transform to detect all straight lines in the image.
- 2) Remove the straight lines that exceed the included angle with the vertical straight line to obtain all straight lines on the cutting edge.
- 3) Calculate the inclination angle of each straight line obtained in step 2, and find their average value.
- 4) Rotation correction according to inclination angle.
- 5) Crop the corrected image.

After the above image correction processing steps, the resulting picture shown in Fig. 11b can be obtained. At this time, the main cutting edge of the image is in a vertical state, which improves the accuracy of subsequent wear value extraction.

It can be seen from the above processing steps that the accuracy of image correction is mainly determined by the threshold set by the Hough transform, where the threshold is the number of sine curves passing through a point in the polar coordinate system. If the threshold is too low, the accuracy is not high, and the straight line on the non-main cutting edge may be mixed, resulting in a correction error. If the threshold is set too high, although the accuracy is improved, the detected straight line may only be a small part of the line segment on the main cutting edge so that in the final corrected image, the main cutting edge may not be in a vertical state. In this paper, after several threshold ranges, the final

**Fig. 11** Image correction. **a** Before calibration. **b** After correction



threshold is determined to be 25, and the Hough transform detection is performed.

### 3.4.2 Wear zone division

Because the edge detected is not an entirely true straight line, the corrected image is jagged at the main cutting edge. In order to reduce the error, the minimum external rectangle method was used to determine the edge of the calculation. In addition, since the blunt tool standard is the width of area B of the tool flank, the wear area is divided into areas C, B, and N in a ratio of 1:2:1, as shown in Fig. 12.

### 3.4.3 Pixel equivalent calibration

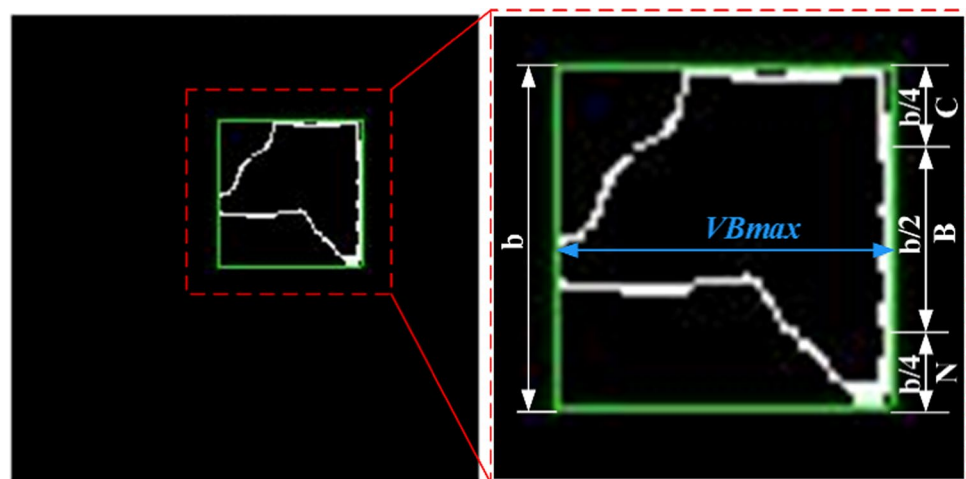
Because of the image obtained at this time, only the wear amount in pixels can be obtained, and the actual value of

tool wear cannot be calculated. Therefore, it is necessary to calibrate the pixel equivalence to obtain the actual wear according to the pixel point. The camera's angle, position, and focus are fixed in image acquisition. Therefore, using the length of the scale as a reference, the ratio of actual scale  $D$  to the total number of  $N$  pixels represented by the scale is calculated as  $k$ , the pixel equivalent of the camera, as follows:

$$k = \frac{D}{N} \quad (7)$$

At this point, a line scan of the tool wear edge image is performed to obtain the number of pixels occupied by each line in the  $B$  area. The number of pixels is then averaged, and the product of the average and pixel equivalent  $k$  is  $VB_{ave}$ , the amount of wear required.

**Fig. 12** Wear area division



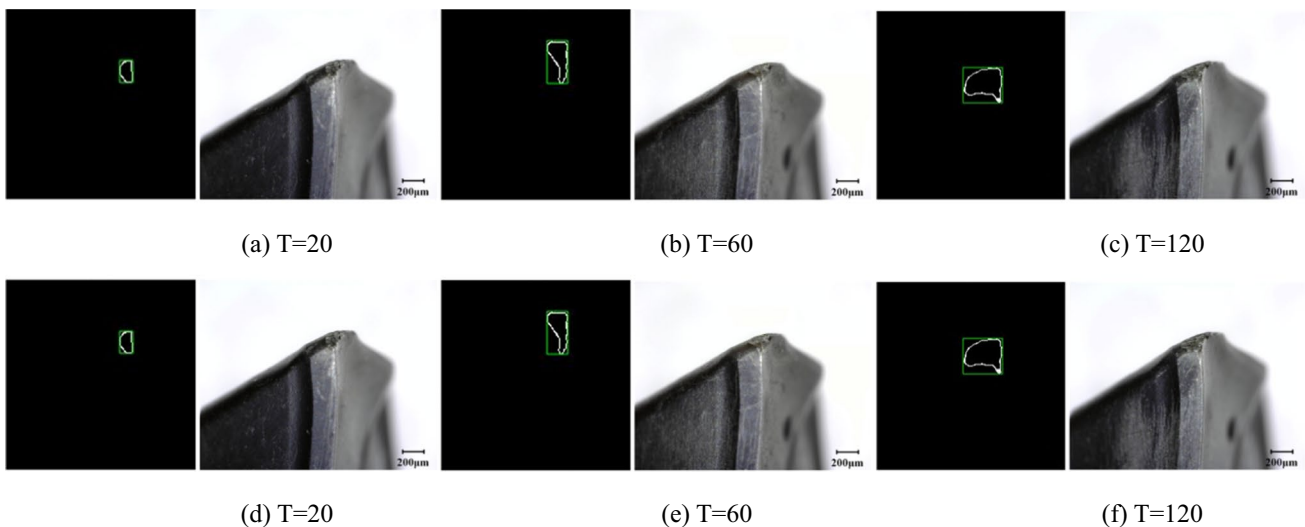


**Fig. 13** **a, b** and **c** are the tool wear images obtained under the cutting condition of ( $v = 40\text{m/min}$ ,  $f_z = 0.15\text{mm/z}$ ), and **d, e**, and **f** are the tool wear images obtained under the cutting condition of ( $v = 60\text{m/min}$ ,  $f_z = 0.2\text{mm/z}$ )

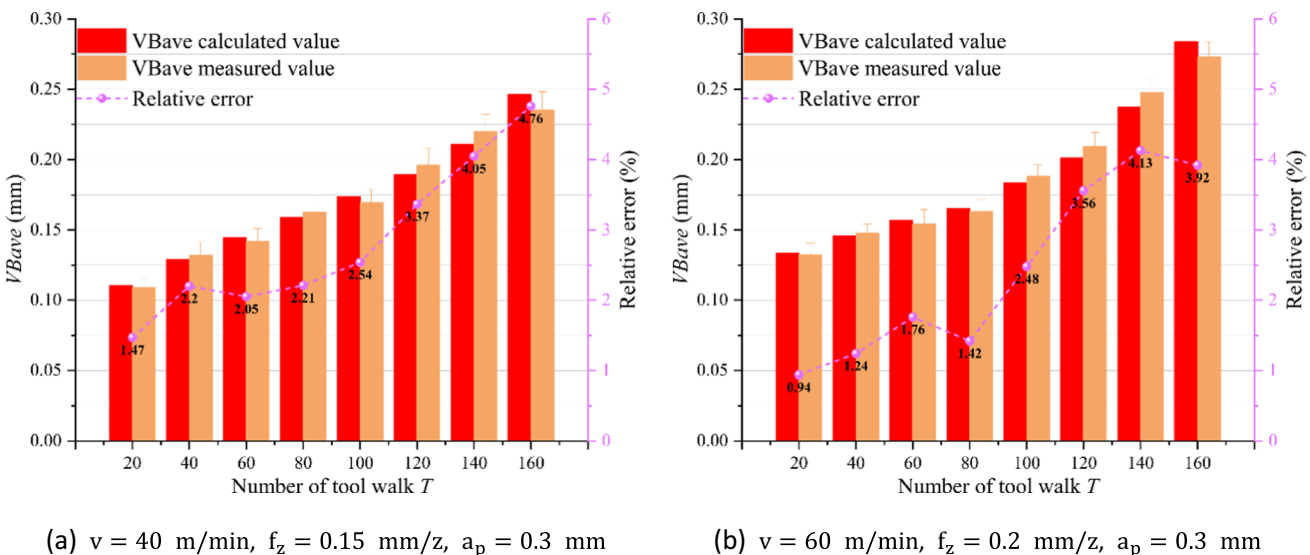


**Fig. 14** Vision module accuracy detection results

### **3.5 Precision detection of visual module**

Figure 13 shows the tool wear conditions observed under three sets of monitoring systems and microscopes extracted from two test results with different cutting parameters. The wear image extracted from the visual monitoring system and the image taken under the microscope is consistent, indicating that the visual module can accurately propose the edge of the wear area.

The comparison between the real wear value of the tool measured under the microscope and the wear value calculated

by the monitoring system is shown in Fig. 14. Under the condition of 16 groups of different cutting parameters, the calculated value and the actual measured value are obtained. The maximum relative error is 4.76%, the maximum error is 0.0112 mm, the minimum relative error is 2.63%, and the minimum error is 0.0012 mm. The average relative error is 2.63%. The experimental results show that with the increase of the number of tool walk  $T$ , the wear degree of the tool deepens and the shape of the wear area become more and more complicated, which leads to the error of wear calculation. Figure 14 shows that the absolute error between the calculated and actual

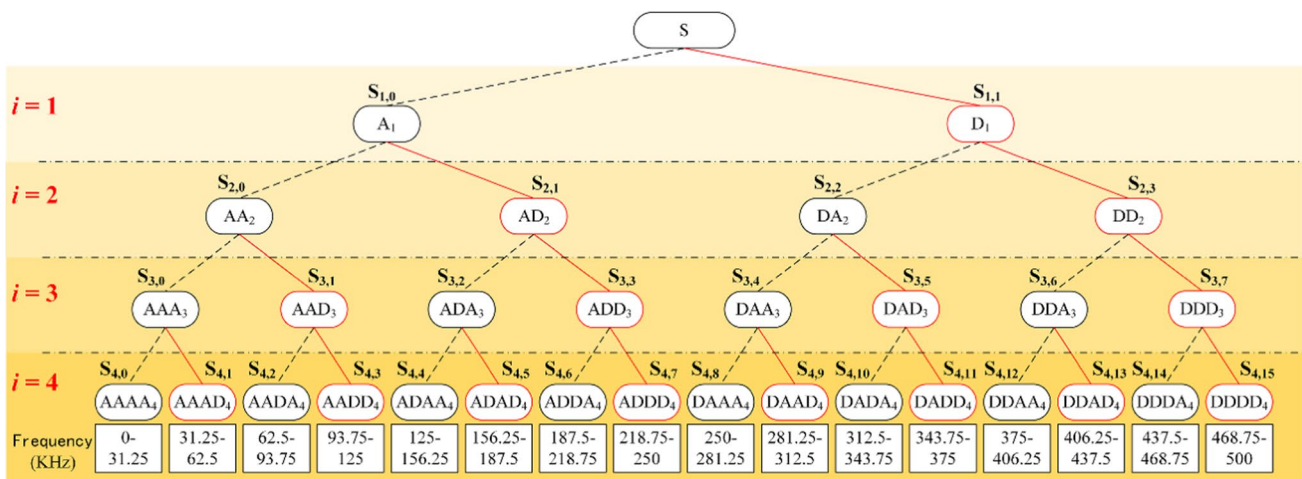


**Fig. 15** Four-layer wavelet packet decomposition schematic

measured values is kept within 5% for all groups. It indicates that the tool wear extracted by the visual module has high reliability under the experimental conditions described in this paper.

## 4 Construction of AE signal feature vector

### 4.1 Preprocessing of AE signal

Since the cutting process is a highly complex dynamic process, it is difficult to avoid all the interference altogether, even if most of the mechanical noises in the AE signal can be filtered by Qualcomm filtering. If the collected AE signal is directly extracted, the unfiltered noise part will affect the model's accuracy. Therefore, to improve the reliability of the subsequent models, it is necessary to preprocess the AE signals obtained by the experiment. In this paper, the collected AE signal is pretreated as follows:

- (1) To remove empty signal segments due to machining gaps.
- (2) Removal of values exceeding more than three times the standard deviation of the signal sample mean.
- (3) A linear term is introduced to remove the trend term introduced by the signal drift.

### 4.2 Feature extraction

#### 4.2.1 Time and frequency domain features extraction

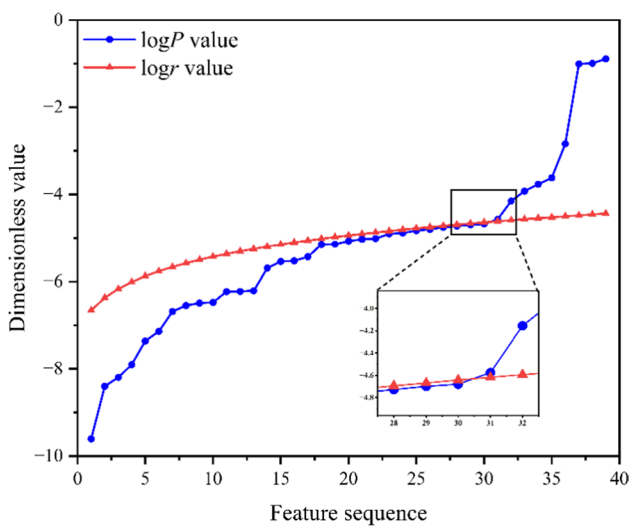
Statistical methods and signal processing techniques are used to extract the signal's time domain and frequency domain features. Ten time domain characteristics of mean, root mean square, maximum amplitude, peak-to-peak value, peak factor,

standard deviation, root amplitude, kurtosis factor, margin factor, and pulse factor can be extracted from AE signals by statistics and calculation. The frequency domain characteristics of AE signals can be extracted by the fast Fourier transform (FFT). The frequency center of gravity and frequency variance is selected here, which can reflect the tool wear condition in the frequency domain.

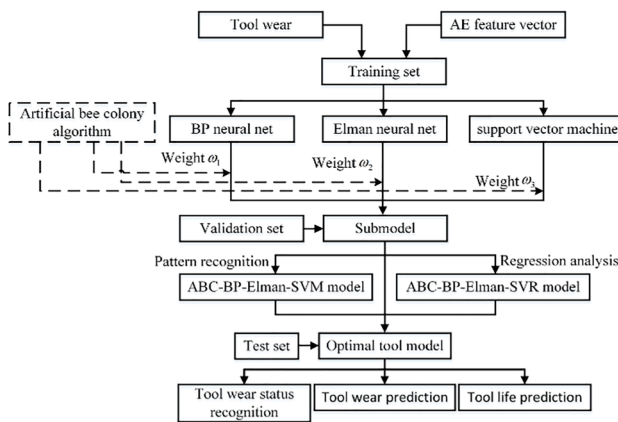
#### 4.2.2 Time–frequency domain features extraction

The AE signal is decomposed by wavelet packet transform (WPT) and empirical mode decomposition (EMD) further to extract time–frequency domain features [26, 27].

In this paper, the wavelet base is selected as db3, and the collected AE signal is decomposed by a 4-layer wavelet. The principle is shown in Fig. 15. In the frequency domain, the



**Fig. 16** Feature screening based on Benjamini-Yekutieli method

**Fig. 17** Tool wear monitoring model

signal is divided into low-frequency and high-frequency two parts by wavelet decomposition, layer by layer decomposition. The signal is decomposed into 16 frequency bands by a 4-layer wavelet.

The energy  $E$  of each frequency band decomposed by the wavelet packet is extracted as the time–frequency domain feature. Its energy can be obtained from the following formula:

$$E_{i,j} = \left| \int S_{4,j}(t) dt \right| = \sum_{m=1}^n |d_{j,m}| \quad (8)$$

where  $d_{j,m}$  ( $j = 1, 2, \dots, 15, m = 1, 2, \dots, n$ ) is the wavelet coefficient of  $S_{4,j}$ . The energy characteristics of 16 frequency bands are extracted by WPT method.

The EMD method decomposes non-stationary signals into a finite sum of intrinsic mode functions (IMF). The signal can be expressed as the sum of  $n$  IMFs and the residual term RES, that is

$$x = \sum_{k=1}^n IMF_k + RES \quad (9)$$

Since the number of IMF components is different for each wear state sample processed by the EMD method, only the first 10 IMFs are retained to ensure that the number of features extracted from each sample is consistent, and the excess IMF components are attributed to RES. Thus, the

**Table 4** BP, Elman neural network parameters

Parameter name	Parameter value
Hidden layer neurons	49
Training times	1000
Training target	$10^{-5}$
Learning rate	0.1

**Table 5** SVM and GA parameters

Parameter name	Parameter value
Penalty factor $C$ range	0.1 ~ 1000
Nuclear parameter	0.1 ~ 1000
Population size $n$	50
Crossover probability $P_c$	0.2
Variation probability $P_m$	0.001
Iteration times $L$	1000

samples decomposed by the EMD method are 10 IMF plus a residual term, namely, 11 components.

### 4.3 Feature screening and fusion

Since not all features correlate with the change of tool wear state, it may lead to feature redundancy, increase computational cost, and affect model accuracy. Therefore, not strongly correlated features need to be filtered [28–30].

The feature screening and fusion algorithm flow used in this paper are as follows:

- (1) Spearman rank correlation test was used to analyze the correlation of all features, the rank correlation coefficient of all features was calculated, and the significant  $P$  value was obtained by looking up the table.
- (2) The false discovery rate (FDR) level value is selected, and  $r$  is calculated according to the Benjamini-Yekutieli method.
- (3) Based on the  $P$  value and  $r$  value, the  $P$  and  $r$  value relationship diagram is drawn, and the feature selection is carried out.
- (4) The filtered features are fused using kernel principal component analysis.

Considering the effectiveness and computational cost of features, the FDR level is selected as 0.05. Taking the logarithm of the  $P$  and  $r$  values, the results are shown in Fig. 16. It can be seen from the graph that under the selected FDR level, the 31st to 39th features are not significantly correlated with the response, so they are filtered out. Filtered

**Table 6** ABC algorithm parameters

Parameter name	Parameter value
Number of employed foragers $n_1$	100
Number of bees observed $n_2$	100
Number of scout bees $n_3$	10
Range of honey source boundary	0 ~ 1
Termination threshold	100
Iteration times $L$	1000

**Fig. 18** Confusion matrix. **a** BP neural network, **b** Elman neural network, **c** SVM, **d** ABC-BP-Elman-SVM

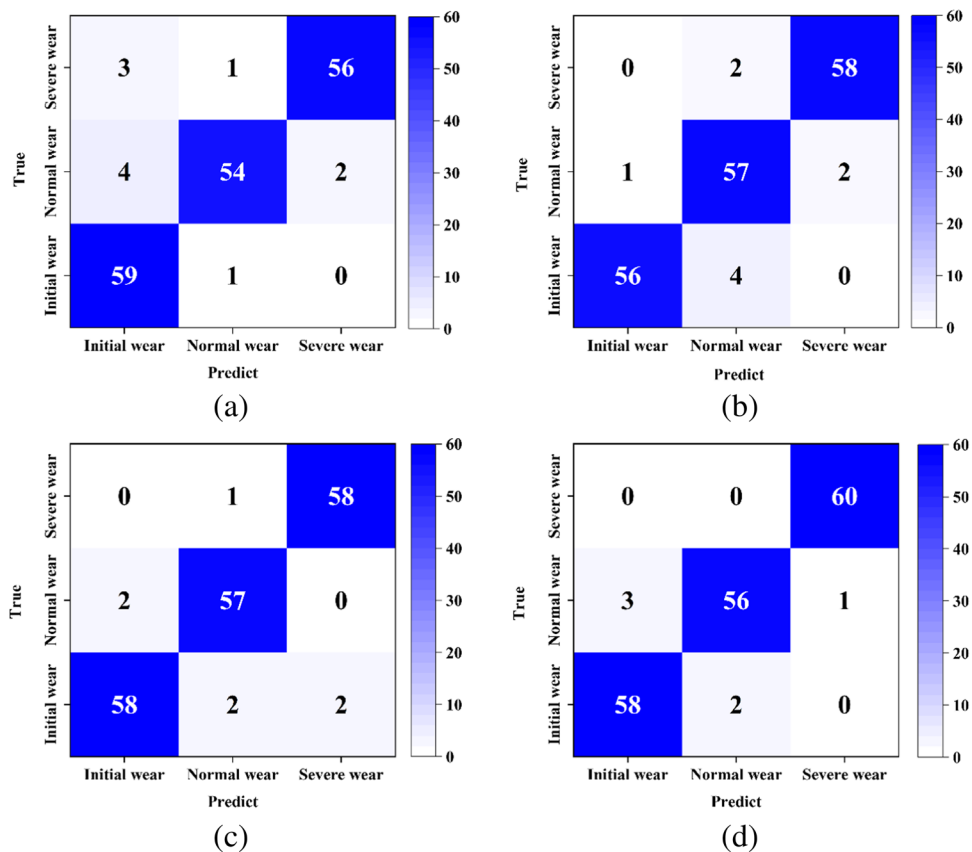


**Fig. 19** Performance of each model on validation set. **a** Recognition accuracy  $A$ , **b** precision ratio  $P$ , **c** recall ratio  $R$ , **d** harmonic mean  $F_1$

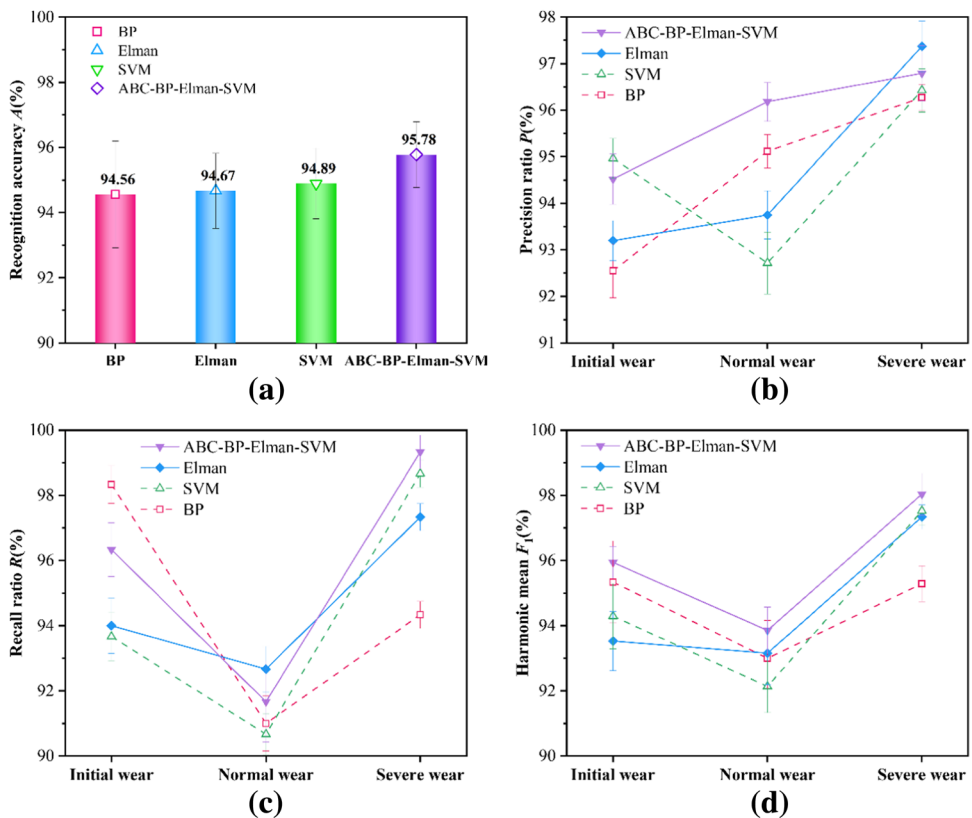


**Table 7** The generalization performance evaluation of ABC-BP-Elman-SVM model

Wear state	Recognition accuracy	Precision ratio	Recall ratio	Harmonic mean
Initial wear	96.11%	95.16%	98.33%	96.72%
Normal wear		98.18%	90%	93.91%
Severe wear		95.24%	100%	97.56%

features are  $E_{4,0}, E_{4,1}, E_{4,2}, E_{4,8}, E_{4,9}, E_{4,10}, E_{4,11}, IMF_9$ , and RES.

## 5 Tool wear monitoring model

### 5.1 Establishment of tool wear monitoring model

Since the sample size of initial wear and severe wear is smaller than that of normal wear, it is necessary to shorten the sampling interval of initial wear and severe wear to balance the sample size of each wear condition. Finally, 300 samples were selected for each wear state; i.e., 900 samples were used for model construction. Samples selected were divided into training, validation, and testing set on a 3:1:1 scale.

The establishment process of the tool wear monitoring model is shown in Fig. 17. BP neural network, Elman neural network, and SVM models were established, respectively, and each model is trained using a training set [31–34]. The trained sub-models were then initially evaluated using a validation set. Based on the performance of each sub-model in the validation set, the ABC algorithm is used to balance the weight of each sub-model, and a combined model is established to minimize the error [35]. According to the application of SVM, the combination model is divided into the ABC-BP-Elman-SVM

recognition model and the ABC-BP-Elman-SVM prediction model. Finally, each sub-model and the combined model are evaluated by the validation set to select the optimal tool model, and the test set evaluates the performance of the optimal model.

BP neural network, Elman neural network, SVM and genetic algorithm (GA), and ABC algorithm parameter settings are shown in Tables 4, 5, and 6, respectively.

### 5.2 Model performance evaluation

#### 5.2.1 Tool wear state recognition model

After training, each sub-model and combined model is validated by ten iterations of the validation set, resulting in a confusion matrix for each model, as shown in Fig. 18.

To compare the performance of each model, four evaluation indexes of recognition accuracy  $A$ , precision ratio  $P$ , recall ratio  $R$ , and harmonic mean  $F_1$  are selected to evaluate the model's performance. According to the confusion matrix of each model, the calculated evaluation results are shown in Fig. 19.

As shown in Fig. 19, the combined ABC-BP-Elman-SVM model has the highest recognition accuracy. The combined model has the highest precision ratio in the normal wear condition and the highest recall ratio in the severe wear condition. The combined model has the highest harmonic mean in all wear conditions. So the combined model has the best overall performance compared to the other models. In

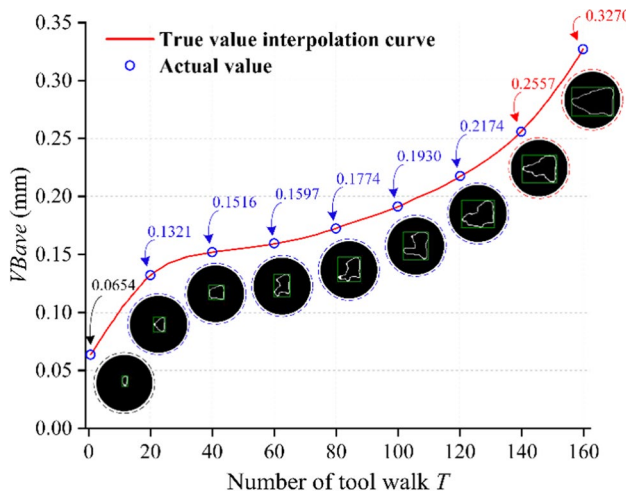


**Fig. 20** Verification set wear fitting curve

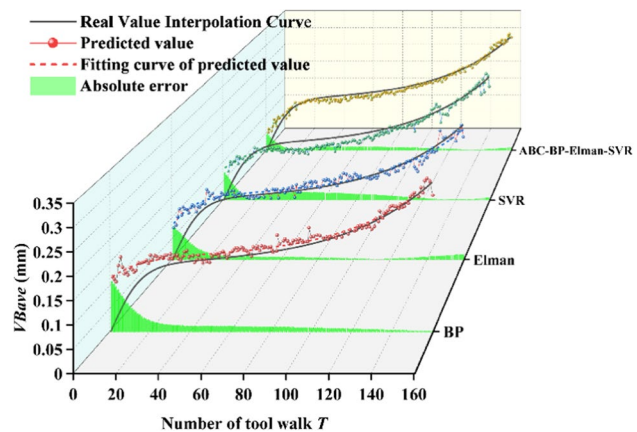


**Fig. 21** Prediction results of tool wear

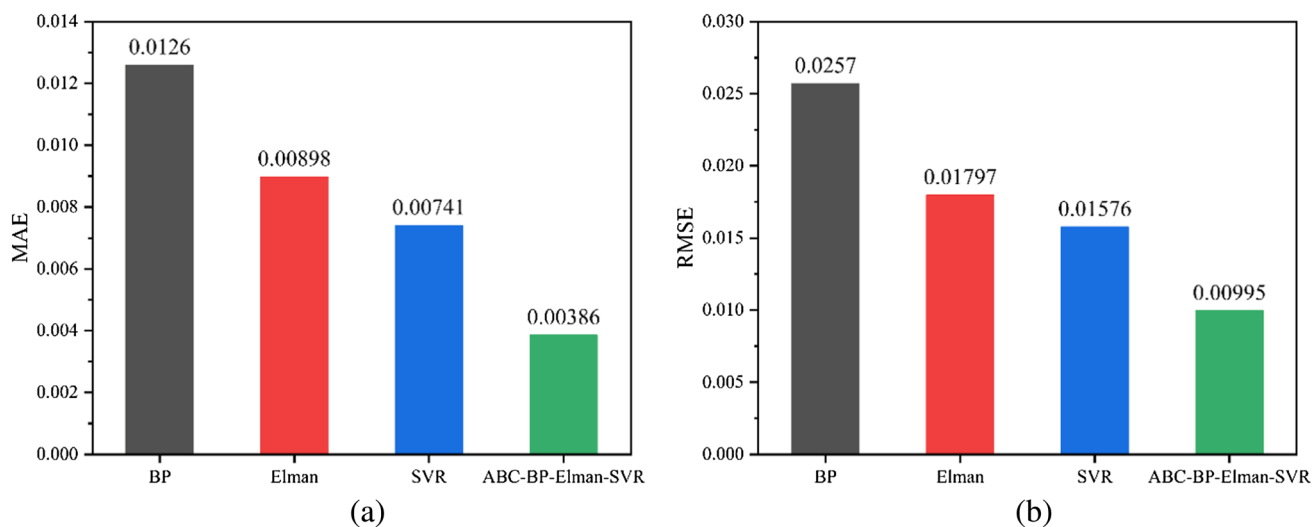


**Fig. 22** The MAE and RMSE of each tool wear prediction model. **a** MAE and **b** RMSE

addition, the combination model has the highest recall ratio in the severe wear condition, which indicates that the combined model has a meager miss-detection rate for the severe wear condition. The combined model is more effective than other models in recognizing the severe wear condition of the tool, which is an integral part of TCM technology.

After determining the optimal model as the ABC-BP-Elman-SVM combined model through the validation set, the test set is used to test the generalization performance of the optimal model. The results are shown in Table 7. All the indexes of the combined model are higher than 90%, of which recognition accuracy is 96.11% and recall ratio of severe wear condition detection is 100%. These results show that the combined model has good generalization performance and can effectively identify different wear states of the tool.

### 5.2.2 Tool wear prediction model

After effectively identifying the tool wear state, the tool wear prediction model is established to accurately grasp the tool wear degree. The actual data of tool wear is obtained by experiment, and the fitting curve of the actual value of the verification set is obtained by fitting, as shown in Fig. 20. The fitted curve runs through all the actual tool wear values, and the curvature does not change suddenly. The obtained curve is consistent with the wear law of the tool. Therefore, this curve is used as the actual wear variation curve and compared with the prediction value of each model. The error value of each model is obtained to verify the prediction performance of each model.

Verify the performance of each model with the validation set to determine the optimal model. The wear prediction results are shown in Fig. 21. As seen from the graph, the prediction results of each model are better excellent. Among

them, the BP and Elma models have significant prediction errors in initial wear. The SVR model has the most significant prediction error in the normal wear phase. The ABC-BP-Elman-SVR combined model has superior prediction results in all wear stages and the best overall prediction performance.

The mean absolute error (MAE) and RMSE for each model are calculated to evaluate each model further, as shown in Fig. 22. As can be seen from the diagram, the MAE and RMSE values of the combined model are the smallest of all models, indicating that the combined model's prediction results are more consistent with experimental data and have better stability.

Through the previous analysis, the optimal model in the predictive model can be identified as the ABC-BP-Elman-SVR combined model. The generalization of the combined model was tested by the test set. The MAE value of the model was obtained as 0.00397, and the RMSE value was 0.0106. As can be seen, the combined model performs as well in the test set as it does in the validation set, which indicates that the model has good generalization performance. In addition, the tool service life can be predicted according to different blunt standards because the prediction model can obtain the tool wear value.

## 6 Conclusion

To effectively and accurately evaluate the tool state, the tool wear state is monitored by combining machine vision and acoustic emission. A general combined tool wear monitoring model is established according to the tool wear characteristic signal obtained from the milling test. The main contributions of this work are as follows.

- (1) A method for automatic online acquisition of tool wear images is proposed. It makes it easier and more efficient to collect images of tool wear areas on the machine.
- (2) The AE signal features are labeled by the tool wear value extracted by machine vision. It makes establishing samples with wear value labels simple and fast.
- (3) The combined tool wear monitoring model was verified and compared with other typical wear monitoring models. The recognition accuracy of the model reached 96.11%, the MAE value of wear prediction was 0.00397, and the RMSE value was 0.0106. The proposed model has high prediction accuracy and good adaptability.

**Acknowledgements** This research has been financially supported by the National Natural Science Foundation of China (No. 51975504, 51475404), the Natural Science Foundation of Hunan Province (No. 2021JJ30676), Provincial Natural Science Foundation of Hunan for Distinguished Young Scholars (2022JJ10045), and Postgraduate Scientific Research Innovation Project of Hunan Province (No. CX20210519, XDCX2022Y103).

**Author contribution** Meiliang Chen performed the experiment and contributed to analysis and manuscript; Mengdan Li contributed to the conception of the study and was a major contributor in writing the manuscript; Linfeng Zhao contributed significantly to analysis and manuscript preparation; Jiachen Liu performed the experiment and wrote the manuscript.

**Funding** This work was supported by the National Natural Science Foundation of China (No. 51975504, 51475404), the Natural Science Foundation of Hunan Province (No. 2021JJ30676), Provincial Natural Science Foundation of Hunan for Distinguished Young Scholars (2022JJ10045), and Postgraduate Scientific Research Innovation Project of Hunan Province (No. CX20210519, XDCX2022Y103).

**Data availability** Some or all data generated or used during the study are available from the corresponding author by request.

**Code availability** Some or all code used during the study are available from the corresponding author by request.

## Declarations

**Ethical approval** Not applicable

**Consent to participate** Not applicable

**Consent to publish** Not applicable

**Competing interests** The authors declare no competing interests.

## References

1. He Z, Shi T, Xuan J (2022) Milling tool wear prediction using multi-sensor feature fusion based on stacked sparse autoencoders. *Measurement* 190:110719. <https://doi.org/10.1016/j.measurement.2022.110719>
2. Mohanraj T, Shankar S, Rajasekar R, Sakthivel NR, Pramanik A (2020) Tool condition monitoring techniques in milling process — a review. *J Mater Res Technol* 9(1):1032–1042. <https://doi.org/10.1016/j.jmrt.2019.10.031>
3. Zhou Y, Zhi G, Chen W, Qian Q, He D, Sun B, Sun W (2022) A new tool wear condition monitoring method based on deep learning under small samples. *Measurement* 189:110622. <https://doi.org/10.1016/j.measurement.2021.110622>
4. Vagnorius Z, Rausand M, Sørby K (2010) Determining optimal replacement time for metal cutting tools. *Eur J Oper Res* 206(2):407–416. <https://doi.org/10.1016/j.ejor.2010.03.023>
5. Liu C, Wang GF, Li ZM (2015) Incremental learning for online tool condition monitoring using Ellipsoid ARTMAP network model. *Appl Soft Comput* 35:186–198. <https://doi.org/10.1016/j.asoc.2015.06.023>
6. Lins RG, Guerreiro B, Marques de Araujo PR, Schmitt R (2020) In-process tool wear measurement system based on image analysis for CNC drilling machines. *IEEE Trans Instrum Meas* 69(8):5579–5588. <https://doi.org/10.1109/TIM.2019.2961572>
7. Shen Y, Yang F, Habibullah MS, Ahmed J, Das AK, Zhou Y, Ho CL (2021) Predicting tool wear size across multi-cutting conditions using advanced machine learning techniques. *J Intell Manuf* 32(6):1753–1766. <https://doi.org/10.1007/s10845-020-01625-7>
8. Li Y, Wang X, He Y, Wang Y, Wang Y, Wang S (2022) Deep spatial-temporal feature extraction and lightweight feature fusion for tool condition monitoring. *IEEE Trans Ind Electron* 69(7):7349–7359. <https://doi.org/10.1109/TIE.2021.3102443>
9. Zamudio-Ramirez I, Antonino-Daviu JA, Trejo-Hernandez M, Osornio-Rios RA (2022) Cutting tool wear monitoring in CNC machines based in spindle-motor stray flux signals. *IEEE Trans Ind Informatics* 18(5):3267–3275. <https://doi.org/10.1109/TII.2020.3022677>
10. Fernández-Robles L, Sánchez-González L, Díez-González J, Castejón-Limas M, Pérez H (2021) Use of image processing to monitor tool wear in micro milling. *Neurocomputing* 452:333–340. <https://doi.org/10.1016/j.neucom.2019.12.146>
11. Zhang T, Zhang C, Wang Y, Zou X, Hu T (2021) A vision-based fusion method for defect detection of milling cutter spiral cutting edge. *Measurement* 177:109248. <https://doi.org/10.1016/j.measurement.2021.109248>
12. Fong KM, Wang X, Kamaruddin S, Ismail MZ (2021) Investigation on universal tool wear measurement technique using image-based cross-correlation analysis. *Measurement* 169:108489. <https://doi.org/10.1016/j.measurement.2020.108489>
13. You Z, Gao H, Guo L, Liu Y, Li J, Li C (2022) Machine vision based adaptive online condition monitoring for milling cutter under spindle rotation. *Mech Syst Signal Process* 171:108904. <https://doi.org/10.1016/j.ymssp.2022.108904>
14. Miao H, Zhao Z, Sun C, Li B, Yan R (2021) A U-Net-based approach for tool wear area detection and identification. *IEEE Trans Instrum Meas* 70:1–10. <https://doi.org/10.1109/TIM.2020.3033457>
15. Dou J, Xu C, Jiao S, Li B, Zhang J, Xu X (2020) An unsupervised online monitoring method for tool wear using a sparse auto-encoder. *Int J Adv Manuf Technol* 106(5–6):2493–2507. <https://doi.org/10.1007/s00170-019-04788-7>
16. Móricz L, Viharos ZJ, Németh A, Szépligeti A, Büki M (2020) Off-line geometrical and microscopic & on-line vibration based cutting tool wear analysis for micro-milling of ceramics. *Measurement* 163:108025. <https://doi.org/10.1016/j.measurement.2020.108025>
17. Kong D, Chen Y, Li N, Tan S (2017) Tool wear monitoring based on kernel principal component analysis and v-support vector regression. *Int J Adv Manuf Technol* 89(1–4):175–190. <https://doi.org/10.1007/s00170-016-9070-x>

18. Laddada S, Si-Chaib MO, Benkedjouh T, Drai R (2020) Tool wear condition monitoring based on wavelet transform and improved extreme learning machine. *Proc Inst Mech Eng Part C J Mech Eng Sci* 234(5):1057–1068. <https://doi.org/10.1177/095440621988544>
19. Gao K, Xu X, Jiao S (2022) Measurement and prediction of wear volume of the tool in nonlinear degradation process based on multi-sensor information fusion. *Eng Fail Anal* 136:106164. <https://doi.org/10.1016/j.englfailanal.2022.106164>
20. Huang Z, Zhu J, Lei J, Li X, Tian F (2020) Tool wear predicting based on multi-domain feature fusion by deep convolutional neural network in milling operations. *J Intell Manuf* 31(4):953–966. <https://doi.org/10.1007/s10845-019-01488-7>
21. Peng R, Liu J, Fu X, Liu C, Zhao L (2021) Application of machine vision method in tool wear monitoring. *Int J Adv Manuf Technol* 116(3–4):1357–1372. <https://doi.org/10.1007/s00170-021-07522-4>
22. Rosten E, Porter R, Drummond T (2010) Faster and better: a machine learning approach to corner detection. *IEEE Trans Pattern Anal Mach Intell* 32(1):105–119. <https://doi.org/10.1109/TPAMI.2008.275>
23. Xiao L, Ouyang H, Fan C (2020) Otsu's thresholding method based on plane intercept histogram and geometric analysis. *Int Arab J Inf Technol* 17(5):692–701. <https://doi.org/10.34028/iajit/17/5/2>
24. Li P (2022) Quantum implementation of the classical Canny edge detector. *Multimed Tools Appl* 81(8):11665–11694. <https://doi.org/10.1007/s11042-022-12337-w>
25. Ershov EI, Terekhin AP, Nikolaev DP (2018) Generalization of the fast Hough transform for three-dimensional images. *J Commun Technol Electron* 63(6):626–636. <https://doi.org/10.1134/S1064226918060074>
26. Barile C, Casavola C, Pappalettera G, Paramasamy KV (2022) Acoustic emission waveforms for damage monitoring in composite materials: shifting in spectral density, entropy and wavelet packet transform. *Struct Heal Monit* 21(4):1768–1789. <https://doi.org/10.1177/14759217211044692>
27. Qu JL, Wang XF, Gao F, Zhou YP, Zhang XY (2014) Noise assisted signal decomposition method based on complex empirical mode decomposition. *Acta Phys Sin* 63(11):110201. <https://doi.org/10.7498/aps.63.110201>
28. Meng Q, Li K, Zhao C (2019) An improved particle filtering algorithm using different correlation coefficients for nonlinear system state estimation. *Big Data* 7(2):114–120. <https://doi.org/10.1089/big.2018.0130>
29. Benjamini Y, Yekutieli D (2001) The control of the false discovery rate in multiple testing under dependency. *Ann Stat* 29(4):1165–1188. <https://doi.org/10.1214/aos/1013699998>
30. Kong D, Zhu J, Duan C, Lu L, Chen D (2021) Surface roughness prediction using kernel locality preserving projection and Bayesian linear regression. *Mech Syst Signal Process* 152:107474. <https://doi.org/10.1016/j.ymssp.2020.107474>
31. Ding S, Su C, Yu J (2011) An optimizing BP neural network algorithm based on genetic algorithm. *Artif Intell Rev* 36(2):153–162. <https://doi.org/10.1007/s10462-011-9208-z>
32. Guo C, Yan J, Tian Z (2019) Analysis and design of an attitude calculation algorithm based on elman neural network for SINS. *Cluster Comput* 22(6):15267–15272. <https://doi.org/10.1007/s10586-018-2562-8>
33. Chauhan VK, Dahiya K, Sharma A (2019) Problem formulations and solvers in linear SVM: a review. *Artif Intell Rev* 52(2):803–855. <https://doi.org/10.1007/s10462-018-9614-6>
34. Guan S, Wang X, Hua L, Li L (2021) Quantitative ultrasonic testing for near-surface defects of large ring forgings using feature extraction and GA-SVM. *Appl Acoust* 173:107714. <https://doi.org/10.1016/j.apacoust.2020.107714>
35. Pu Q, Xu C, Wang H, Zhao L (2022) A novel artificial bee colony clustering algorithm with comprehensive improvement. *Vis Comput* 38(4):1395–1410. <https://doi.org/10.1007/s00371-021-02367-0>

**Publisher's Note** Springer Nature remains neutral with regard to jurisdictional claims in published maps and institutional affiliations.

Springer Nature or its licensor (e.g. a society or other partner) holds exclusive rights to this article under a publishing agreement with the author(s) or other rightsholder(s); author self-archiving of the accepted manuscript version of this article is solely governed by the terms of such publishing agreement and applicable law.